Differential role of nonmuscle myosin II isoforms during blebbing of MCF-7 cells

Sumit K. Dey[a,†,‡], Raman K. Singh[a,†], Shyamtanu Chattoraj[b], Shekhar Saha[a,§], Alakesh Das[c], Kankan Bhattacharyya[b], Kaushik Sengupta[d], Shamik Sen[c], and Siddhartha S. Jana[a,*]

[a]Department of Biological Chemistry and [b]Department of Physical Chemistry, Indian Association for the Cultivation of Science, Jadavpur, Kolkata 700032, India; [c]Department of Biosciences and Bioengineering, Indian Institute of Technology–Bombay, Mumbai 400076, India; [d]Biophysics and Structural Genomics Division, Saha Institute of Nuclear Physics, Kolkata 700064, India

ABSTRACT **Bleb formation has been correlated with nonmuscle myosin II (NM-II) activity. Whether three isoforms of NM-II (NM-IIA, -IIB and -IIC) have the same or differential roles in bleb formation is not well understood. Here we report that ectopically expressed, GFP-tagged NM-II isoforms exhibit different types of membrane protrusions, such as multiple blebs, lamellipodia, combinations of both, or absence of any such protrusions in MCF-7 cells. Quantification suggests that 50% of NM-IIA-GFP–, 29% of NM-IIB-GFP–, and 19% of NM-IIC1-GFP–expressing MCF-7 cells show multiple bleb formation, compared with 36% of cells expressing GFP alone. Of interest, NM-IIB has an almost 50% lower rate of dissociation from actin filament than NM-IIA and –IIC1 as determined by FRET analysis both at cell and bleb cortices. We induced bleb formation by disruption of the cortex and found that all three NM-II-GFP isoforms can reappear and form filaments but to different degrees in the growing bleb. NM-IIB-GFP can form filaments in blebs in 41% of NM-IIB-GFP–expressing cells, whereas filaments form in only 12 and 3% of cells expressing NM-IIA-GFP and NM-IIC1-GFP, respectively. These studies suggest that NM-II isoforms have differential roles in the bleb life cycle.**

Monitoring Editor
Manuel Théry
CEA, Hopital Saint Louis

Received: Jul 20, 2016
Revised: Jan 26, 2017
Accepted: Feb 21, 2017

INTRODUCTION

Blebs are membrane protrusions or bulges that appear and disappear from the surface of a cell in a repetitive asynchronous manner that is induced by localized decoupling of the plasma membrane from the cortex. The cortex is a specialized layer of cytoplasm composed of actin filaments, nonmuscle myosin II (NM-II), and other associated proteins (Alberts *et al.*, 2002; Pesen and Hoh, 2005). Blebbing is a common phenomenon observed during cytokinesis (Fishkind *et al.*, 1991; Boucrot and Kirchhausen, 2007), spreading (Bereiter-Hahn *et al.*, 1990; Pletjushkina *et al.*, 2001), migration (Trinkaus, 1973; Friedl and Wolf, 2003; Sahai and Marshall, 2003; Blaser *et al.*, 2006), viral infection (Mercer and Helenius, 2008), and the execution phase of apoptosis (Robertson *et al.*, 1978; Mills *et al.*, 1998; Coleman *et al.*, 2001) of animal cells. Blebbing is also one of the modes adopted by cancer cells for their migration during tissue invasion (Sahai and Marshall, 2003; Wolf *et al.*, 2003). Bleb-mediated migration is known as amoeboid migration. Studies in cancer cells have demonstrated that cells with high Rho activity correlate with amoeboid migration, whereas high Rac1 activity often displays mesenchymal motility (Parri and Chiarugi, 2010). Rac1 is a key regulator of protrusive actin polymerization, whereas Rho promotes actomyosin contractility. Actomyosin contractility generates membrane tension inside the cell during cellular motility. Consequently Rho and its downstream effector ROCK induce blebbing through increased actomyosin contractility and may play role in a signaling pathway that induces bleb-based motility during cell migration (Yap and Kovacs, 2003; Takesono *et al.*, 2010).

Once a bleb is nucleated, it grows by filling with cytosol and forms a quasihemispherical protrusion that initially remains devoid of actin and other cytoskeletal structures. Expansion of the bleb

This article was published online ahead of print in MBoC in Press (http://www.molbiolcell.org/cgi/doi/10.1091/mbc.E16-07-0524) on March 1, 2017.

†These authors contributed equally.

Present addresses: ‡Yale University, 219 Prospect St., New Haven, CT 06511-2106; §Department of Biochemistry and Molecular Genetics, University of Virginia, Charlottesville, VA 22904.

*Address correspondence to: Siddhartha S. Jana (bcssj@iacs.res.in).

Abbreviations used: ELC, essential light chain; FRET, fluorescence resonance energy transfer; NM-II, nonmuscle myosin II; NMHC-II, nonmuscle myosin heavy chain II; RLC, regulatory light chain.

eventually slows as sufficient cytosolic liquid is not supported by the contractile force of the cortex in the bleb, which is needed to maintain the constant growth rate of growing bleb, and as the bleb membrane undergoes a transition from a lipid bilayer to cortex formation with cytoskeleton (Cunningham, 1995). During this transition, first membrane–actin linker proteins such as ezrin/radixin/moesin (ERM) and then actin are recruited at the bleb membrane. A cage-like structure is formed underneath the bleb membrane called de novo cortex. Soon thereafter, actin-bundling proteins such as α-actinin, coronin, and fimbrin are recruited and assemble into the bleb cortex. Finally, proteins of the contractile system such as tropomyosin followed by NM-II are recruited to the bleb cortex and power bleb retraction (Charras *et al.*, 2006).

Variation of actomyosin contractility depends on the different biochemical properties of NM-II isoforms, such as MgATPase activity, in vitro motility, and duty ratio (Kovacs *et al.*, 2003; Wang *et al.*, 2003; Kim *et al.*, 2005; Heissler and Manstein, 2011). NM-II has three isoforms, referred as NM-IIA, NM-IIB, and NM-IIC, based on their heavy chains, which are encoded by three different genes, MYH9, MYH10, and MYH14, respectively (Katsuragawa *et al.*, 1989; Shohet *et al.*, 1989; Takahashi *et al.*, 1992; Golomb *et al.*, 2004). NM-IIs are hexameric proteins composed of two heavy chains of 230 kDa, two regulatory light chains of 20 kDa (RLC20), and two essential light chains of 17 kDa (ELC17). Depending on tissue and cell type, NM-II isoforms have distinct roles during embryonic development (Wang *et al.*, 2011) and functional redundancy in cell division and neuritogenesis (Saha *et al.*, 2013). However, their roles in maintaining the differential contractility or tension within cells to control bleb dynamics are poorly understood.

Here we demonstrate for the first time that the ectopically expressed NM-IIA isoform can promote more bleb protrusions than NM-IIB and NM-IIC1 isoforms in MCF-7 cells. Further, we show that at both cell and bleb cortices, NM-IIB has a lower dissociation rate from actin filaments than NM-IIA and NM-IIC1. In laser-induced blebs, we find that the NM-IIB isoform forms more filaments in the early steps of bleb expansion than do the NM-IIA and NM-IIC1 isoforms.

RESULTS

NM-IIs promote different types of membrane protrusions in MCF-7 cells

Previous studies reported that the three isoforms of NM-II have different biochemical properties. To determine whether these different biochemical properties can be correlated with different membrane protrusive activities, we ectopically expressed each NM-II isoform tagged with green fluorescent protein (GFP) in human breast tumor cells, MCF-7, which endogenously express substantial amounts of each isoform of NM-II (Smutny *et al.*, 2010). GFP-positive cells were monitored for membrane protrusions using time-lapse confocal microscopy over a period of 20 min (≥95 cells for each construct). Note that we used GFP-tagged NM-IIC1, an alternatively spliced isoform of NM-IIC, which is the only isoform expressed in MCF-7 cells (Jana *et al.*, 2006). Quantification revealed that control cells (MCF-7 cells expressing only GFP) exhibited three major types of membrane protrusions: multiple blebs (36% of total cells), lamellipodia (42%), and no protrusion (14%; Figure 1, A and C, Supplemental Movies S1–S3, and Table 1). Cells with both multiple blebs and lamellipodia protrusions were less abundant (only 8%). The formation of multiple blebs was increased to 50% when NM-IIA-GFP was expressed in the cells (Supplemental Movie S4), whereas it was reduced to 29 and 19% when NM-IIB-GFP and NM-IIC1-GFP were ectopically expressed in MCF-7 cells, respectively (Figure 1, B and C, and Table 1). Multiple blebs were characterized if at a given time point more than one bleb was formed at different positions throughout the cell periphery. Another membrane protrusion, lamellipodia formation, was increased to 65% in NM-IIC1-GFP–expressing cells (Supplemental Movie S5), compared with NM-IIA-GFP and NM-IIB-GFP cells, which showed only 24 and 39%, respectively (Figure 1, B and C, and Table 1). Of interest, no such membrane protrusion was observed in 26% of NM-IIB-GFP–expressing MCF-7 cells (Supplemental Movie S6), compared with 2% of NM-IIA-GFP– and 9% of

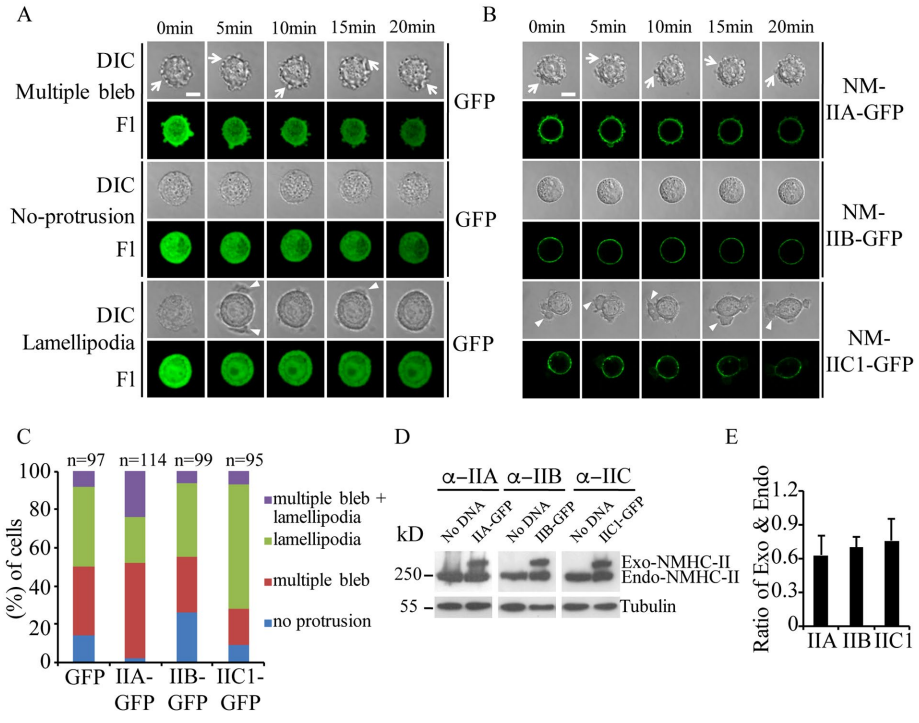

FIGURE 1: (A, B) Time-lapse images of multiple blebs, no protrusions, or lamellipodia-forming MCF-7 cells expressing GFP alone (A) or each of the NM-II-GFP isoforms (B). Fluorescence (Fls) images below DIC images at each time point. Multiple blebs (top two rows) are denoted by white arrows and lamellipodia by white arrowheads (bottom two rows). Scale bar, 10 μm. (C) Quantification of cells exhibiting different types of membrane protrusions in cells expressing NM-IIA-GFP, NM-IIB-GFP, NM-IIC1GFP, or GFP. Note that NM-IIA increases multiple bleb formation and NM-IIC1 lamellipodia formation. The data represent ≥95 cells for each sample from three independent experiments. (D) Lysates of MCF-7 cells transfected with each of the NMHC-II-GFP–encoding plasmid DNAs or no DNA were probed with NMHC-II isoform–specific antibodies as indicated. Tubulin was used as loading control. One representative blot from three independent experiments. Note that exogenous NMHC-II-GFP migrates more slowly than endogenous NMHC-IIs. (E) Ratio of (exogenous/endogenous bands) of individual isoforms is calculated from relative band intensity of exo-NMHC-II-GFP/relative band intensity of endo-NMHC-II of the same isoform.

		Multiple blebs (%)	Lamellipodia (%)	No protrusion (%)	Both multiple blebs and lamellipodia (%)
Overexpression	GFP	36	42	14	8
	IIA-GFP	50	24	2	24
	IIB-GFP	29	39	26	6
	IIC1-GFP	19	65	9	7
Knockdown	NS siRNA	28	51	15	6
	IIA siRNA	11	66	14	9
	IIB siRNA	49	11	35	5
	IIC siRNA	47	15	28	10

MCF-7 cells were transfected with each of the GFP-tagged NM-II isoforms or 50 nM siRNA against each isoform. Data represent ≥95 cells for each GFP construct and ≥37 cells for each siRNA from three independent experiments.

TABLE 1: Percentages of MCF-7 cells showing different types of membrane protrusions.

NM-IIC1-GFP–expressing cells (Figure 1, B and C, and Table 1). The percentage of cells showing both multiple blebs and lamellipodia remained the same (6–8%), except for NM-IIA-GFP cells, which showed 24%, suggesting formation of multiple blebs in lamellipodia-forming cells. In parallel, movies taken up to 120 min showed that NM-II-GFP–positive cells, which showed multiple blebs and no protrusion or lamellipodia, were less likely to exhibit interchangeability with other types of membrane-protrusive activity (Supplemental Figure S1). We checked the expression level of ectopically expressed NM-IIs and found that the amounts of exogenous NM-IIs were 60–70% of the endogenous level of NM-IIs in MCF-7 cells (Figure 1, D and E). Bleb-forming cells were not apoptotic (Supplemental Figure S2). These results indicate that NM-IIA induces multiple bleb protrusion and NM-IIC1 induces lamellipodia, whereas multiple blebs or lamellipodia formation was not affected by overexpression of NM–IIB, suggesting differential roles among NM-II isoforms in membrane protrusions of MCF-7 cells.

To explore further the role of individual isoforms in membrane protrusions, we inhibited the expression of each isoform using small interfering RNA (siRNA) and then analyzed cells with time-lapse video microscopy. Figure 2A shows that siRNA targeting nonmuscle myosin heavy chain IIA (NMHC-IIA) specifically reduced the amount of NM-IIA (compare lane 2 with lane 1) by 40% but did not reduce NM-IIB or NM-IIC. Similarly, reducing NM-IIB by 49% with NMHC-IIB siRNA (lane 3) or reducing NM-IIC by 52% with NMHC-IIC siRNA (lane 4) did not affect the expression of other isoforms. Quantification of membrane protrusions in siRNA-treated cells (Figure 2B and Table 1) revealed that multiple bleb formation was reduced to 11% in IIA-siRNA–treated cells, whereas it was increased to 49 and 47% in IIB- and IIC-siRNA cells, respectively. Of interest, lamellipodia formation was increased to 66% in NM-IIA–knockdown cells, whereas it was reduced to 11 and 15% in NM-IIB– and NM-IIC–knockdown cells, respectively, compared with control cells treated with nonspecific siRNA, which showed 28% multiple blebs and 51% lamellipodia, suggesting that NM-IIB and NM-IIC play opposite roles to NM-IIA in multiple blebs and lamellipodia formation. The increase of the no-protrusion result in NM-IIB and NM-IIC siRNA–treated cells may be attributed to a decrease in lamellipodia formation, which was the most abundant phenotype in control cells. The increase in the cell population with both multiple blebs and lamellipodia formation in NM-IIA-GFP–expressing cells occurred due to formation of multiple blebs most likely in lamellipodial cells. Taken together, these results suggest that overexpression or knockdown of NM-II isoforms leads to imbalances in the membrane-protrusive activities of MCF-7 cells.

NM-IIA-GFP–expressing cells exhibit a higher fluctuation rate during blebbing

Our previous result suggests that bleb protrusion events that are increased in ectopically expressing NM-IIA cells can also be seen in ectopically expressing NM-IIB and NM-IIC1 cells (Figure 1C and Table 1). To understand how bleb protrusion is phenotopically different among cells expressing different NM-II isoforms, we characterized bleb protrusion using MATLAB analysis. We captured time-lapse confocal images at 5-s intervals for >20 min in multiple-bleb-forming cells that expressed NM-IIA-GFP, NM-IIB-GFP, NM-IIC1-GFP, or GFP alone. We drew contour outlines along the cell edge and measured the edge fluctuation at each time point. Figure 3A shows the multiple-bleb-forming cells and the contour of the cells expressing each isoform. MCF-7 cells expressing only GFP fluctuated at a rate of 8.7 ± 2.5 $\mu m^2/s$ (11 cells). In contrast, NM-IIA-GFP–expressing MCF-7 cells exhibited a higher fluctuation rate of 16.2 ± 5.8 $\mu m^2/s$ (20 cells) than with the other isoforms, NM-IIB-GFP and NM-IIC1-GFP, which showed fluctuation rates of only 8.2 ± 2.3 (10 cells) and 10.3 ± 2.8 $\mu m^2/s$ (nine cells), respectively (Figure 3, B and C, and Supplemental Movies S7–S10). These results suggest that multiple bleb protrusions may be correlated with the higher fluctuation rate of NM-IIA-GFP–expressing cells. In parallel, fluorescence time-lapse images showed loss of fluorescence intensity of each NM-II isoform at the cell cortex, where a bleb is formed due to the NM-II contractile effect (Supplemental Figure S3). Taken together, these data experimentally validate the previous hypothesis of cortex breakage and resealing–induced bleb formation and retraction (Paluch *et al.*, 2005).

Previous results prompted us to examine why NM-IIA-GFP–expressing cells showed a higher cell edge/periphery fluctuation than NM-IIB-GFP– and NM-IIC1-GFP–expressing cells during blebbing. We measured the cortical stiffness of cells using atomic force microscopy (AFM) and found that NM-IIA-GFP–expressing cells showed high cortical stiffness (1.46 ± 0.17 kPa, $n = 20$) compared with cells expressing NM-IIB-GFP ($n = 22$) or IIC1-GFP ($n = 20$), which showed 0.82 ± 0.12 and 0.89 ± 0.12 kPa, respectively (Figure 3D). These results suggest that the NM-IIA isoform induces higher cortical stiffness, which may be attributed to increase cell edge/periphery fluctuation compared with NM-IIB and NM-IIC1 isoforms.

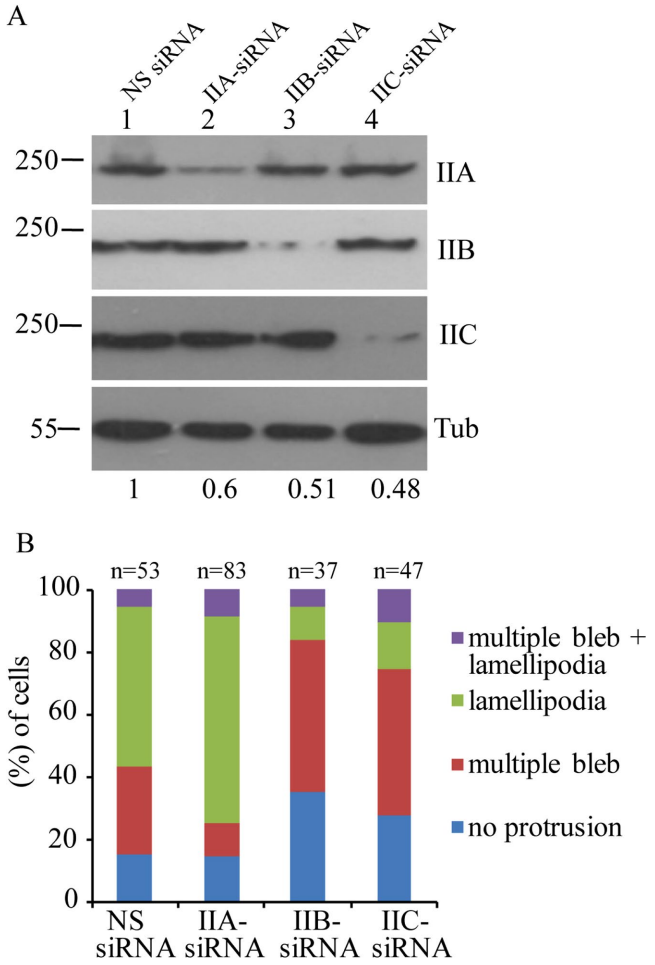

FIGURE 2: (A) Lysates from MCF-7 cells transfected with nonspecific (NS) siRNA (lane 1), NM-IIA-siRNA (lane 2), NM-IIB-siRNA (lane 3), or NM-IIC-siRNA (lane 4) were subjected to immunoblot with antibodies as indicated. Tubulin was used as a loading control. Bottom, relative band intensity of NM-II isoform in siRNA-treated cells calculated by considering the band intensity of that NM-II isoform in NS siRNA–treated cells as 1. One representative blot from three independent experiments. (B) Quantification of cells exhibiting different types of membrane protrusions in cells treated with IIA-siRNA, IIB-siRNA, IIC-siRNA, or NS siRNA. Note that the percentage of multiple bleb formation is reduced in IIA siRNA–treated cells, formation of lamellipodia is reduced in IIC siRNA–treated cells, and multiple bleb formation is increased in IIB siRNA–treated cells compared with NS siRNA–treated cells. The data represent ≥37 cells of each sample from three independent experiments.

NM-IIB exhibits longer dwell time than NM-IIA and NM-IIC1 at the cell cortex

Contractility of the actomyosin complex at the cell cortex generates breakage and resealing of the cortex, which leads to formation and retraction of blebs. Contractility is dependent on the interaction between NM-II filaments with actin filaments. Variations of contractility may depend on the binding ability of individual NM-II isoforms with the actin filaments. To measure the binding or dissociation kinetics of individual NM-II molecules with actin filaments in the cortex of a live cell, we carried out fluorescence resonance energy transfer (FRET) analysis at the cortex of MCF-7 cells that were cotransfected with GFP-tagged NM-II isoforms and Lifeact-RFP, a marker of filamentous actin (Riedl *et al.*, 2008). First, we checked the FRET efficiency at the cell cortex for low emission intensity of donor (GFP-tagged NM-II isoforms) and high emission intensity of acceptor (red fluorescent protein [RFP]–tagged actin), shown in Supplemental Figure S4A, and changes in FRET intensity with respect to time, shown in Supplemental Figure S4B. Figure 4, A–C, shows the distribution of FRET efficiency of actomyosin complexes involving NM-II-GFP isoforms and RFP-actin at the cell cortex. The majority of the NM-IIs exhibit high FRET efficiency ($\varepsilon_{FRET} > 0.5$), suggesting that the majority of each NM-II isoform is in close proximity to actin filaments, which may be due to formation of the actomyosin complex between each NM-II-GFP and LifeAct-RFP at the cell cortex. We measured the dwell time of each NM-II isoform, which determines the binding time with the actin filament, inversely correlated with the rate of dissociation from the actin filament. Figure 4, D–F, shows that all of the isoforms exhibit two dwell times at high FRET. The dwell-time distribution was fitted with the convolution of two exponentials. We found one shorter average dwell time (τ_1), 33 ± 2 s (50% of total dwell-time distribution [TDTD]), and one longer average dwell time (τ_2), 60 ± 5 s (50% of TDTD), for NM-IIA-GFP, whereas those for NM-IIB-GFP and NM-IIC1-GFP were τ_1 = 35 ± 3 s (35% of TDTD) and τ_2 =110 ± 5 s (65% of TDTD), and τ_1 = 35 ± 2 s (40% of TDTD) and τ_2 = 70 ± 5 s (60% of TDTD), respectively. Of interest, the faster component of the average dwell time (τ_1) in each isoform does not change, but the slower component of average dwell time (τ_2) doubles times for the NM-IIB isoform compared with the NM-IIA and NM-IIC1 isoforms. The amplitude value of each dwell time indicates that >50% of the population of each isoform has a lower dissociation rate ($1/\tau_2 \leq 1/60\ s^{-1}$), and the population with a significant amount of NM-IIB possesses a lower dissociation rate ($<1/110\ s^{-1}$) than those with NM-IIC1 and NM–IIA ($<1/70$ and $<1/60\ s^{-1}$, respectively). These data suggest that the three isoforms of NM-II have different rates of dissociation from actin filaments in the order NM-IIA > NM-IIC1 > NM-IIB, which may be contributing to different rates of contractility at the cell cortex.

NM-IIB exhibits a longer dwell time than NM-IIA and NM-IIC1 at the bleb cortex

The de novo bleb cortex is formed by the stepwise appearance of ERM, actin, and actin-associated proteins on a time scales of seconds. Finally, NM-II is recruited to the bleb cortex and powers bleb retraction. To initiate bleb retraction, ~50 myosins are needed, and almost fivefold more myosin motors are recruited by the end of the bleb retraction process (Charras *et al.*, 2008). Therefore variations of contractility will be different for individual NM-II isoforms with actin filaments during this dynamic remodeling process. To measure the binding/dissociation kinetics of individual NM-II molecules with actin filaments in a live bleb cortex, we carried out FRET analysis at the bleb cortex of cells that coexpressed GFP-tagged NM-II and Lifeact-RFP. We found the same FRET efficiency at the de novo bleb cortex in terms of low emission intensity of donors (GFP-tagged NM-II isoform) and high emission intensity of acceptors (RFP-tagged actin) as at the cell cortex. However, in terms of changes in FRET intensity with respect to time, the bleb cortex differs from the cell cortex (Supplemental Figure S4C). Figure 5, A–C, shows the distribution of FRET efficiency of the actomyosin complex for each NM-II isoform and actin at the bleb cortex. We found more than one FRET efficiency at the bleb cortex, indicating that NM-II and actin in the bleb cortex exist at more than one distance, which may be attributed to the dynamic remodeling of de novo cortex. Dwell-time analysis revealed that when NM-IIs are at a distal position (low FRET efficiency, $\varepsilon_{FRET} < 0.5$) with respect to actin filaments, they all showed a similar rate of dissociation (τ = 85 ± 3 s for NM-IIA, 86 ± 3 s for

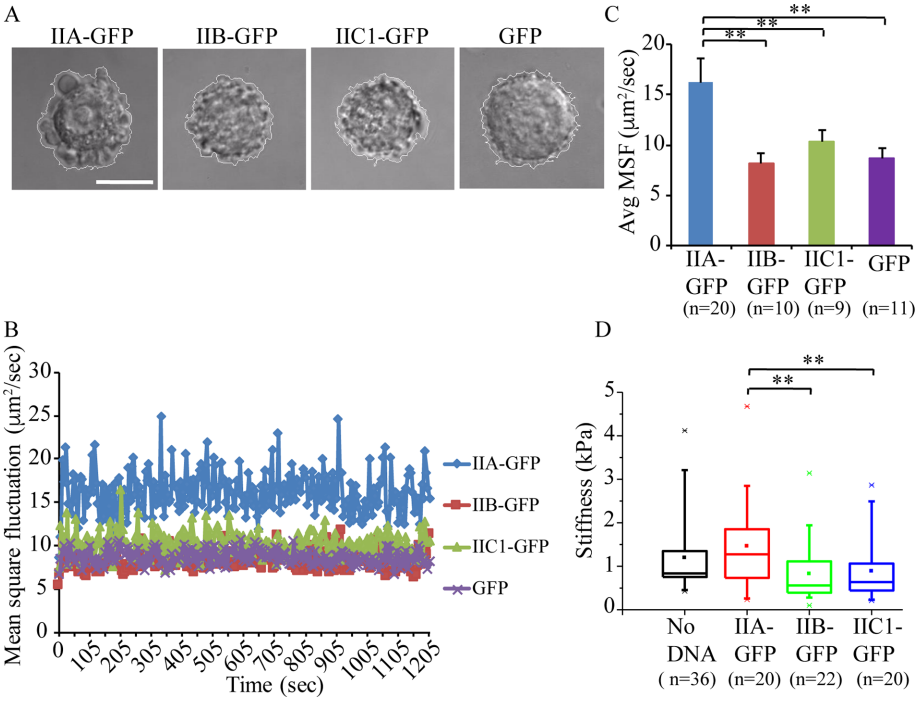

FIGURE 3: (A) Contour over the cell edge expressing NM-IIA-GFP, NM-IIB-GFP, NM-IIC1-GFP, or GFP alone. Images were captured at 5-s interval for 20 min of each type of NM-IIs-GFP–expressing cell. Fluctuation was calculated by measuring the movement of the contour using MATLAB software. (B) MSF vs. time plot and (C) its average for MCF-7 cells expressing NM-IIA-GFP, NM-IIB-GFP, NM-IIC1-GFP, and GFP alone. The data represent mean ± SD from three independent experiments. $^{**}p < 0.05$ for NM-IIA-GFP vs. NM-IIB-GFP, NM-IIC1-GFP, and GFP alone. (D) Stiffness of MCF-7 cells expressing each of the NM-II-GFPs using AFM. The boxes represent the 25th and 75th percentiles, the horizontal lines indicate the median, the small dots indicate the mean, and the whiskers indicate SD. The data are from three independent experiments. $^{**}p < 0.05$ for NM-IIA-GFP vs. NM-IIB-GFP or NM-IIC1-GFP.

NM-IIB, 90 ± 3 s for NM-IIC1; Figure 5, D–F). In contrast, when they are close to actin filaments (high FRET efficiency, $\varepsilon_{FRET} > 0.5$), the rate of dissociation differed among NM-IIs ($\tau = 46 \pm 3$ s for NM-IIA, 93 ± 3 s for NM-IIB, 50 ± 3 s for NM-IIC1; Figure 5, G–I). NM-IIB has a lower dissociation rate (<1/93 s^{-1}) than NM-IIC1 and NM-IIA (<1/50 and <1/46 s^{-1}, respectively). These results suggest that even in the bleb cortex, NM-IIB has a similar differential interaction behavior (different rates of dissociation from actin filaments) to that at the cell cortex in the order NM-IIA > NM-IIC1 > NM-IIB.

Filament formation by NM-IIB at cortex-ablated blebs

The hypothesis of Paluch *et al.* (2005) and Supplemental Figure S3 predicts that cortex breakage induces bleb formation and that blebs are retracted within 2–3 min. To study the role of NM-IIs in bleb dynamics, we induced nonretractive bleb formation by laser-mediated cortex ablation, for which the size of the cortex breakage was significantly larger than a cell's autonomous blebs. We analyzed nonprotrusive MCF-7 cells for cortex breakage and found that all type of cells expressing different types of NM-II isoforms were able to induce multiple bleb formation. Multiple bleb formation was an abundant phenotype (>70%; Supplemental Figure S5A) in cortex-ablated cells. We performed time-lapse confocal imaging over 20 min of nonretracted blebs (>50 cells), which originated at the site of laser ablation. All of the NM-II isoforms could reappear as clusters of fluorescence at the void region of the growing bleb during bleb expansion after cortex disruption and form filament-like structures to different degrees. Figure 6, A–C, shows that NM-IIB-GFP could form filaments in nonretracted blebs within 5 min (Supplemental Movie S12), whereas in most cases, NM-IIA and NM-IIC1 were inefficient in forming filaments until 20 min (Supplemental Movies S11 and S13). Quantification revealed that 41% of NM-IIB-GFP–expressing cells showed filament formation, whereas only 12% of cells expressing NM-IIA-GFP and 3% of cells expressing NM-IIC1-GFP showed filament formation (Figure 6D). We measured the area of bleb expansion (at the site of laser-mediated cortex ablation) at each time point and found that the initial area was almost same, whereas later, it was increased in cells expressing NM-IIA-GFP (315 ± 86 μm^2, nine cells) or NM-IIC1-GFP (353 ± 95 μm^2, 10 cells). In contrast, the area of bleb expansion halted in NM-IIB-GFP–expressing cells (206 ± 49 μm^2, nine cells) after 10 min (Figure 6E). These data suggest that the rate of filament assembly of NM-IIB is higher than that of NM-IIA and NM-IIC1 in the multiple blebs induced by cortex ablation, which may serve as a barrier for further bleb expansion after 10 min. We measured the kinetics of bleb expansion of each of NM-II isoform expressing MCF-7 cells using kymograph analysis. Supplemental Figure S5, B and C, shows the images of blebs at $t = 0$ and 20 min, respectively. One of the representative kymographs of bleb expansion from each isoform-expressing cell is shown in Supplemental Figure S5D. At the initial period, bleb expansion shows global membrane ruffling with cells expressing NM-IIA-GFP or NM-IIC1-GFP, whereas no such event was observed in NM-IIB-GFP–expressing cells, which may be attributed to the periodic contraction by NM-IIB-GFP. This initial time period of bleb expansion of each isoform-expressing cell is magnified and shown in Supplemental Figure S5E. In addition, NM-IIB-GFP colocalized with actin filaments in the growing bleb after cortex ablation in MCF-7 cells coexpressing NM-IIB-GFP and LifeAct-RFP (Supplemental Figure S6). Taken together, these data suggest that both bleb formation and bleb expansion are limited by NM-IIB activity, which can be explained as being due to its longer dwell time with actin filaments at both cell and bleb cortices.

DISCUSSION

We demonstrated that the membrane protrusion activity of a cell can be altered by changing the amount of individual NM-II isoforms. Understanding the membrane protrusion activity of cancer cells is of great importance. Using time-lapse confocal microscopy and biochemical assay, we reveal that although NM-IIA and NM-IIC1 have opposite roles in formation of blebs and lamellipodia, both can induce cancer cell phenotypes, either amoeboid or mesenchymal, which are needed for optimum migration during metastasis.

Bergert *et al.* (2012) showed that the protrusive activity of the cell can be fine-tuned by the complexity of the environment. Walker carcinoma cells exhibited bleb and lamellipodia protrusions when they were in suspension and adherent environments, respectively. Cells having myosin-driven lower cortical tension favor lamellipodia

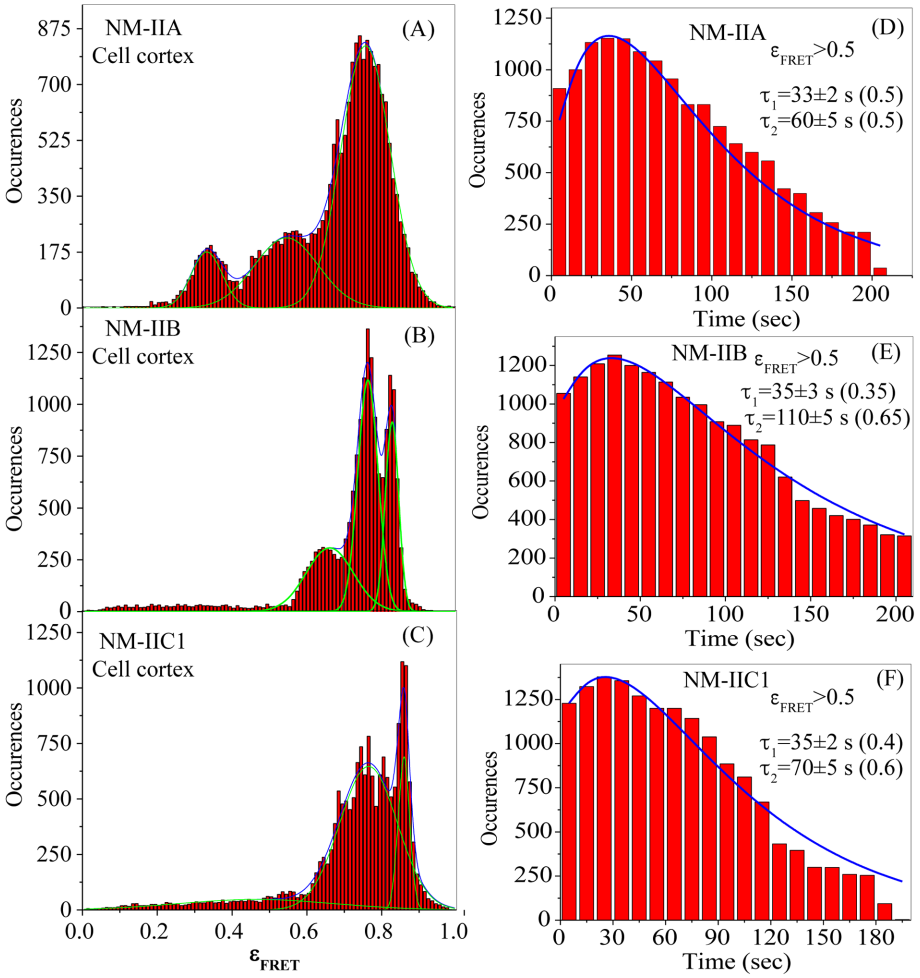

FIGURE 4: FRET efficiency between each NM-II-GFP isoform and LifeAct-RFP was determined at the cell cortex in MCF-7 cells. Histograms of FRET for GFP-tagged (A) NM-IIA, (B) NM-IIB, or (C) NM-IIC1 with RFP-tagged actin at the cell cortex. The dwell-time distributions of the high-FRET states of (D) NM-IIA, (E) NM-IIB, or (F) NM-IIC1 with actin. Note that each NM-II isoform contains both shorter and longer dwell times at high-FRET states. Although the shorter dwell times for each isoform are quite similar, the longer dwell time of NM-IIB is higher than with NM-IIA or NM-IIC1 at the cell cortex. Data represent >20 events from 8–10 cells.

formation, whereas high cortical tension favors bleb formation. Because three isoforms of NM-II have different biochemical properties, we asked whether changing the amount of each NM-II isoform (by its ectopic expression) can induce switching between bleb and lamellipodia formation. Overexpression of NM-IIA induced blebs and of NM-IIC1 induced lamellipodia, whereas knockdown of NM-IIA reduced blebs and that of NM-IIC and NM-IIB reduced lamellipodia but induced bleb formation, suggesting that switching between bleb and lamellipodia formation can be modulated by the amount of NM-II isoforms in actomyosin complex in a cancer cell, and a critical amount of NM-IIB may act as barrier to multiple bleb formation. Differential membrane protrusive activity of MCF-7 cells may be attributed to different degrees of cortical stiffness. NM-IIA-GFP–expressing cells have higher cortical stiffness, which provides a relative measure of cortical tension (Salbreux *et al.*, 2012) for blebs, whereas NM-IIC1-GFP– and NM-IIB–GFP–expressing cells have a lower cortical stiffness (Figure 3D) for lamellipodia formation. Higher cortical stiffness/tension makes the cortex more contractile and generates more breakage and resealing events on a time scale of milliseconds at the cortex, which could be the outcome of higher cell edge/periphery fluctuation in the case of NM-IIA-GFP–expressing cells (Figure 3, B and C).

The question arises of why NM-IIA induces bleb formation. NM-IIA displays higher in vitro motility, as it propels actin filament approximately two to three times faster than NM-IIB or NM-IIC1 (Pato *et al.*, 1996; Kovacs *et al.*, 2007; Heissler and Manstein, 2011). In addition, NM-IIA belongs to a lower–duty ratio motor family, as it binds to the actin filaments weakly compared with NM-IIB and NM-IIC1 (Kovacs *et al.*, 2003; Rosenfeld *et al.*, 2003). NM-IIA slides over the actin at a faster rate and hence may be responsible for exerting higher cortical stiffness and hence tension in MCF-7 cells, which promotes multiple bleb protrusion.

Tinevez *et al.* (2009) hypothesized that laser ablation mimics endogenous bleb nucleation by local disruption of the cortex. They showed that local disruption of the actin cortex using laser ablation leads to the formation of a membrane bleb. The induced blebs were spherical in shape and devoid of intracellular structures, similar to blebs that naturally occur in cells. They also showed that size and growth of a bleb were strongly dependent on cortical tension, which drove the expansion of the bleb. Charras *et al.* (2006) showed that NM-II reappeared and formed a continuous rim structure, which powered bleb retraction. Similarly, we performed laser ablation at the cell cortex to induce bleb nucleation. On ablation, NM-IIs reappeared in the bleb, but NM-IIB-GFP–expressing cells induced filament assembly in the growing bleb more rapidly than NM-IIA-GFP– and NM-IIC1-GFP–expressing cells and resisted bleb expansion (Figure 6E). NM-IIA-GFP– and NM-IIC1-GFP–expressing cells exhibited global membrane ruffling, whereas NM-IIB-GFP–expressing cells exhibited periodic contraction during initial bleb expansion. This could be explained by the slower in vitro motility rate and higher duty ratio of NM-IIB than with NM-IIA and NM-IIC1. NM-IIB has a significantly higher duty ratio of ~23–40% (Wang *et al.*, 2003) or 82% (Rosenfeld *et al.*, 2003), and NM-IIA has a duty ratio of ~10% (Kovacs *et al.*, 2003). The higher duty ratio of NM-IIB suggests that NM-IIB molecules spend a much longer time in the actin-binding state and, consequently, NM-IIB requires less time to reassemble in the bleb and subsequently form filaments during bleb growth. This physical property indicates that NM-IIB plays an important role in tension generation and force maintenance, in contrast to NM-IIA.

We hypothesize that changing the membrane protrusion activity by a cell might be possible by selective activation of NM-II isoforms by different signaling pathways (Rho or Rac) or replacing one with another NM-II isoform in an actomyosin complex. Previous studies suggest that bleb dynamics is controlled by a signaling cascade mediated by Rho/ROCK/NM-II in which the small GTPase Rho recruits and activates ROCK to phosphorylate the myosin light chain, thereby inducing myosin contraction and an increase in

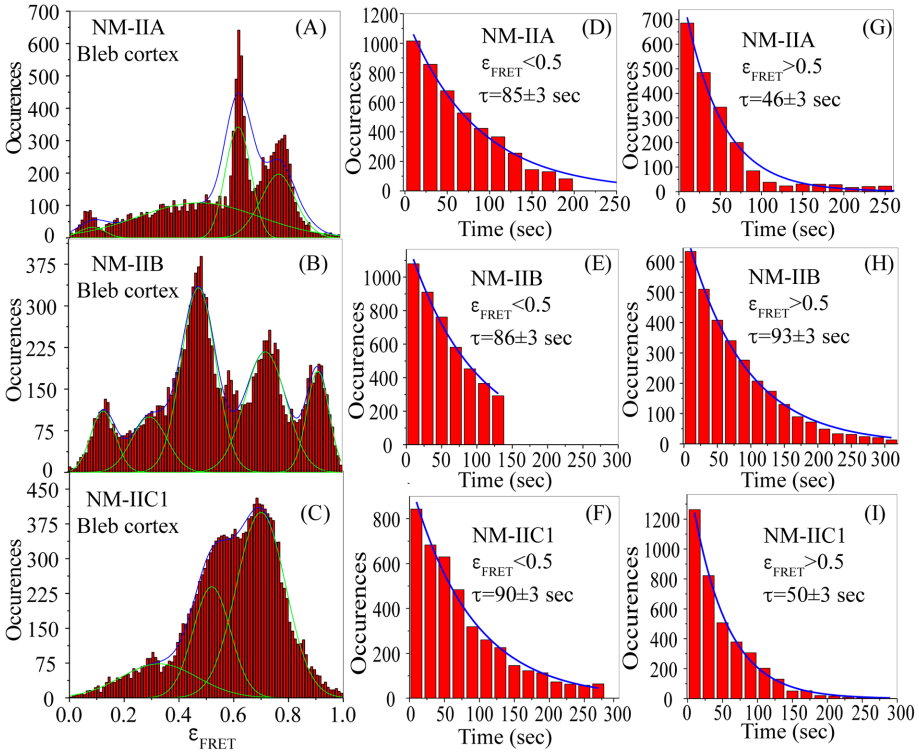

FIGURE 5: FRET efficiency of each NM-II-GFP isoform and LifeAct-RFP was carried out at the de novo bleb cortex in MCF-7 cells. Histograms of FRET occurrence of GFP-tagged (A) NM-IIA, (B) NM-IIB, or (C) NM-IIC1 with RFP-tagged actin at the bleb cortex. The dwell-time distributions of the low-FRET states of (D) NM-IIA, (E) NM-IIB, or (F) NM-IIC1 with actin. The dwell-time distributions of the high-FRET states of (G) NM-IIA, (H) NM-IIB, or (I) NM-IIC1 with actin. Note that, although the dwell times of the low-FRET states the NM-II isoforms are quite similar, the dwell time of the high-FRET state for NM-IIB is longer than with NM-IIA or NM-IIC1 in the bleb cortex. Data represent >20 events from 8–10 cells.

local intracellular pressure (Mills *et al.*, 1999; Coleman *et al.*, 2001; Yarrow *et al.*, 2005). In this context, we carried out time-lapse imaging analysis of MCF-7 cells expressing GFP-tagged, wild-type RLC, a phosphomimic form, or its phosphodead form. Both wild-type and phosphomimic forms increased multiple bleb formation (Supplemental Figure S7), whereas phosphodead form to lamellipodia, confirming the involvement of this signaling pathway in regulating NM-II activity in membrane protrusions in MCF-7 cells. Further study is needed to understand the signaling pathways involved in regulation of NM-II isoform–specific activity during lamellipodia dynamics, but our study shows the importance of NM-II isoforms in migratory modes, which may help in developing therapeutic strategies for more effective inhibition of tumor cell migration.

MATERIALS AND METHODS

DNA and siRNA transfection

The human nonmetastatic breast tumor cell line MCF-7 was purchased from the American Type Culture Collection (Manassas, VA) and grown in DMEM high-glucose supplemented with 10% fetal bovine serum, 1% penicillin/streptomycin/glutamine, and 10 μg/ml insulin (Sigma-Aldrich, St. Louis, MO). A 1-μg amount of plasmid DNA or 50 nM siRNA was transfected into 2×10^5 MCF-7 cells using Lipofectamine 2000 (Thermo Fisher Scientific, Waltham, MA). siRNA sequences were designed against the 3′-untranslated region: sense, 5′-GCUCAGAAUCUGAUACCAA [dT][dT], and antisense, 5′-UUGGUAUCAGAUUCUGAGC [dT][dT], for NMHC-IIA; sense, 5′-GGCAAUACAGUGGGACAGU [dT][dT], and antisense, 5′-ACUGUCCCACUGUAUUGCC [dT][dT], for NMHC-IIB; and sense, 5′-CCUCGUUAUUGAUCUAUAG [dT][dT], and antisense, 5′-CUAUAGAUCAAUAACGAGG [dT][dT], for NMHC-IIC (Thermo Fisher Scientific). A nonspecific siRNA duplex (SIC001) was obtained from Sigma-Aldrich.

SDS–PAGE and immunoblotting

Lysates of MCF-7 cells transfected with 1 μg of plasmid DNA or 50 nM siRNA were run on SDS–PAGE 6% polyacrylamide Tris-glycine gels and transferred to a polyvinylidene fluoride membrane. The membrane was blocked in phosphate-buffered saline containing 5% skim milk and 0.05% Tween-20 and incubated with antibody specific to each NM-II isoform or tubulin overnight at 4°C. The blots were washed and incubated with secondary antibody conjugated with horseradish peroxidase for 2 h at room temperature, followed by the addition of Super-Signal Femto reagent (Thermo Fisher Scientific). The luminescence signal was captured on Kodak x-ray film, and band intensity was quantified by ImageJ software (National Institutes of Health, Bethesda, MD).

Cell imaging, laser ablation, image processing, and data analysis

Time-lapse cell imaging of membrane protrusions was performed on a confocal laser scanning microscope equipped with eclipse Ti-E, Plan Apochromat VC 60×/1.4 oil Objective, and Digital Sight DS-Qi1MC monochromatic camera, supported by the NIS-AR software (Nikon, Tokyo, Japan). Images were recorded at 20-s intervals for 20 min using a 488-nm continuous-wave multiline Ar gas laser with an estimated 200-μW power at the point of the sample. All time-lapse imaging was performed under 5% CO_2 and at 37°C in a stage incubator (INU-TIZ-F1; Nikon). Laser ablation of the cortex was performed using a 405-nm continuous-wave (He diode) laser with an estimated 340-μW power at the point of the sample for 5 s (Tinevez *et al.*, 2009). The region of interest for laser ablation was set at 1.5 μm^2 and pinhole size 60 mm. After ablation, subsequent differential interference contrast (DIC) and fluorescence images were captured using a 488-nm laser. Images were processed with ImageJ. They were rotated and cropped, and their contrast and brightness were manually adjusted. To calculate the mean-squared fluctuation (MSF) of cell-edge velocity, we performed imaging at 5-s intervals for 20 min for each GFP-tagged NM-II isoform and analysis using MATLAB software (MathWorks; Giannone *et al.*, 2007), using the equation $MSF(t, \theta) = \langle\{c(t, \theta) - c(t + 1, \theta)\}^2\rangle\theta$.

Atomic force microscopy

MCF-7 cells were transfected with plasmid DNA encoding GFP-tagged NMHC-IIA, -IIB, or -IIC1. Culture dishes were mounted onto the stage of an Asylum MFP3D atomic force microscope (Asylum Research) coupled to a Zeiss epifluorescence microscope and indented using a pyramid-tipped probe (Olympus) with nominal

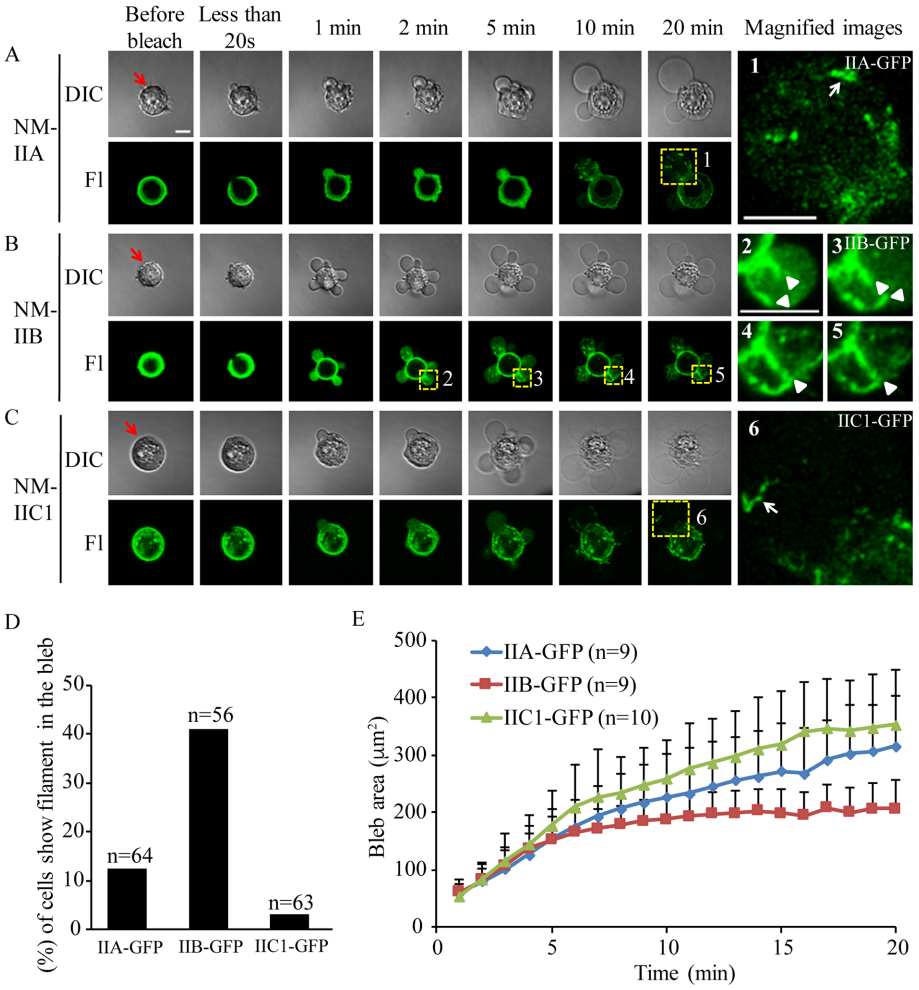

FIGURE 6: Time-lapse images of MCF-7 cells expressing NM-IIA-GFP (A), NM-IIB-GFP (B), or NM-IIC1-GFP (C) after cortex ablation at the indicated time points. Fluorescence (Fl) images are shown below the DIC image at each time point. Red arrows denote the cortex ablation site in each cell. Magnified images of yellow rectangular regions are shown in right column of each NM-II isoform at different time points as indicated by the numerals. Note that NM-IIB-GFP forms filaments in the bleb, as shown by white arrowheads; clusters of fluorescence formed by NM-IIA-GFP and NM-IIC1-GFP are shown by white arrows in the magnified images. Scale bar, 10 μm. (D) Quantification of cells expressing NM-IIA-GFP, NM-IIB-GFP, or NM-IIC1-GFP that form filaments in a bleb after cortex ablation. Note that NM-IIB-GFP–expressing cells show the maximum number of filaments formed in the bleb. (E) Area of the bleb (at the site of laser-mediated cortex ablation) in cells expressing each isoform was measured for 20 min (≥9 cells). Note that the bleb area of NM-IIA-GFP– or NM-IIC1-GFP–expressing cells is progressively increased throughout time, whereas that of NM-IIB-GFP–expressing cells is stationary for 10 min after cortex ablation. Data represent three independent experiments.

spring constant of 20 pN/nm. GFP-positive cells were selected for the measurements, which were done in a stretch of the membrane where there was no protrusion. Actual spring constants were estimated using a thermal calibration method, and force curves were recorded for >20 cells for each sample. Force–indentation profiles were fit with a modified Hertzian model of a cone indenting a semi-infinite elastic material to extract the magnitude of cortical stiffness (MacKay and Kumar, 2013).

Experimental setup and data analysis for FRET

Emission spectra, confocal microscope, and FRET. The steady-state emission spectra of fluorophores were recorded in MCF-7 cells using an electron-multiplying charge-coupled device (ANDOR Technology) and a spectrograph (Shamrock series; ANDOR Technology). The spectrograph was attached to one of the ports of a PicoQuant MicroTime 200 apparatus. The confocal microscope setup (MicroTime 200) with an inverted optical microscope (Olympus IX-71) was described previously (Chowdhury *et al.*, 2013). The donor (GFP) was excited at 470 nm using a picosecond diode with stable repetition rate (40 MHz). The power of the exciting laser was kept at 1 μW during FRET measurements. The fluorescence signal was separated from the exciting laser with a dichroic mirror (490DCXR; Chroma) and appropriate band-pass filters (HQ500lp; Chroma). The donor and acceptor fluorescence signals were detected separately using a dichroic mirror (540DCLP) and two detectors (micro photon device). Two additional band-pass filters (FF01-520/35 for the donor and 600-nm band pass for the acceptor) were used to further separate the donor and acceptor fluorescence.

The single-molecule efficiency of FRET (ε_{FRET}) was calculated from

$$\varepsilon_{FRET} = \frac{I_A}{\gamma I_D + I_A} \quad (1)$$

where I_A and I_D are the background- and cross-talk–corrected acceptor and donor intensities, respectively. The correction factor γ was described earlier (Chowdhury *et al.*, 2013).

The distance between the dye pairs (R_{DA}) was calculated from

$$R_{DA} = R_0 \left[\frac{1-E}{E}\right]^{\frac{1}{6}} \quad (2)$$

where R_0 is the Förster distance. The FRET efficiency histograms were generated from 10 individual data sets of three different experiments.

Dwell-time analysis. The single-molecule time traces were processed using a binning time of 100 ms. The dwell times of both high- and low-FRET states were determined using Origin 6 software. The FRET states for which ε_{FRET} values were <0.5 are described as low-FRET states, and those for which ε_{FRET} values were > 0.5 are described as high-FRET states. In both cases, a cut-off ε_{FRET} value of 0.1 was used to eliminate the contribution of donor-only populations in the dwell-time analysis. Each dwell-time histogram was constructed from 10 individual data sets of three different experiments.

Statistical analysis

Data are expressed as mean ± SD. Statistical significance was tested with Student's *t* test, and the level of significance was taken as $p < 0.05$.

ACKNOWLEDGMENTS

We thank R. Chisholm (Northwestern University, Chicago, IL) and Hidde Ploegh (Whitehead Institute for Biomedical Research, Cambridge, MA) for kind gifts of RLC-GFP and LifeAct-RFP plasmids, respectively. We thank Deepak K. Sinha (Indian Association for the Cultivation of Science) and Mary Anne Conti (National Heart, Lung, and Blood Institute) for reading the manuscript and Sinha for helping in MATLAB data analysis. S.D. thanks the Council of Scientific and Industrial Research and the Indian Association for the Cultivation of Science for the award of a fellowship. This work was supported by the Department of Science and Technology (EMR/2015/002054), Government of India.

REFERENCES

Alberts B, Alexander J, Lewis J, Raff M, Roberts K, Walter P (2002). Molecular Biology of the Cell, 4th ed., New York: Garland.

Bereiter-Hahn J, Luck M, Miebach T, Stelzer HK, Voth M (1990). Spreading of trypsinized cells: cytoskeletal dynamics and energy requirements. J Cell Sci 96, 171–188.

Bergert M, Chandradoss SD, Desai RA, Paluch E (2012). Cell mechanics control rapid transitions between blebs and lamellipodia during migration. Proc Natl Acad Sci USA 109, 14434–14439.

Blaser H, Reichman-Fried M, Castanon I, Dumstrei K, Marlow FL, Kawakami K, Solnica- Krezel L, Heisenberg C-P, Raz E (2006). Migration of zebrafish primordial germ cells: a role for myosin contraction and cytoplasmic flow. Dev Cell 11, 613–627.

Boucrot E, Kirchhausen T (2007). Endosomal recycling controls plasma membrane area during mitosis. Proc Natl Acad Sci USA 104, 7939–7944.

Charras GT, Coughlin M, Mitchison TJ, Mahadevan L (2008). Life and times of a cellular bleb. Biophys J 94, 1836–1853.

Charras GT, Hu C-K, Coughlin M, Mitchison TJ (2006). Reassembly of contractile actin cortex in cell blebs. J Cell Biol 175, 477–490.

Chowdhury R, Chattoraj S, Mojumdar SS, Bhattacharyya K (2013). FRET between a donor and an acceptor covalently bound to human serum albumin in native and non-native states. Phys Chem Chem Phys 15, 16286–16293.

Coleman ML, Sahai EA, Yeo M, Bosch M, Dewar A, Olson MF (2001). Membrane blebbing during apoptosis results from caspase-mediated activation of ROCK I. Nat Cell Biol 3, 339–345.

Cunningham CC (1995). Actin polymerization and intracellular solvent flow in cell surface blebbing. J Cell Biol 129, 1589–1599.

Fishkind DJ, Cao LG, Wang YL (1991). Microinjection of the catalytic fragment of myosin light chain kinase into dividing cells: effects on mitosis and cytokinesis. J Cell Biol 114, 967–975.

Friedl P, Wolf K (2003). Tumor-cell invasion and migration: diversity and escape mechanisms. Nat Rev Cancer 3, 362–374.

Giannone G, Dubin-Thaler BJ, Rossier O, Cai Y, Chaga O, Jiang G, Beaver W, Dobereiner H-G, Freund Y, Borisy G, Sheetz MP (2007). Lamellipodial actin mechanically links myosin activity with adhesion-site formation. Cell 128, 561–575.

Golomb E, Ma X, Jana SS, Preston YA, Kawamoto S, Shoham NG, Goldin E, Conti MA, Sellers JR, Adelstein RS (2004). Identification and characterization of nonmuscle myosin II-C, a new member of the myosin II family. J Biol Chem 279, 2800–2808.

Heissler SM, Manstein DJ (2011). Comparative kinetic and functional characterization of the motor domains of human nonmuscle myosin-2C isoforms. J Biol Chem 286, 21191–21202.

Jana SS, Kawamoto S, Adelstein RS (2006). A specific isoform of nonmuscle myosin II-C is required for cytokinesis in a tumor cell line. J Biol Chem 281, 24662–24670.

Katsuragawa Y, Yanagisawa M, Inoue A, Masaki T (1989). Two distinct nonmuscle myosin-heavy-chain mRNAs are differentially expressed in various chicken tissues. Identification of a novel gene family of vertebrate non-sarcomeric myosin heavy chains. Eur J Biochem 184, 611–616.

Kim K-Y, Kovacs M, Kawamoto S, Sellers JR, Adelstein RS (2005). Disease-associated mutations and alternative splicing alter the enzymatic and motile activity of nonmuscle myosins II-B and II-C. J Biol Chem 280, 22769–22775.

Kovacs M, Thirumurugan K, Knight PJ, Sellers JR (2007). Load-dependent mechanism of nonmuscle myosin 2. Proc Natl Acad Sci USA 104, 9994–9999.

Kovacs M, Wang F, Hu A, Zhang Y, Sellers JR (2003). Functional divergence of human cytoplasmic myosin II: kinetic characterization of the non-muscle IIA isoform. J Biol Chem 278, 38132–38140.

MacKay JL, Kumar S (2013). Measuring the elastic properties of living cells with atomic force microscopy indentation. Methods Mol Biol 931, 313–329.

Mercer J, Helenius A (2008). Vaccinia virus uses macropinocytosis and apoptotic mimicry to enter host cells. Science 320, 531–535.

Mills JC, Stone NL, Erhardt J, Pittman RN (1998). Apoptotic membrane blebbing is regulated by myosin light chain phosphorylation. J Cell Biol 140, 627–636.

Mills JC, Stone NL, Pittman RN (1999). Extranuclear apoptosis: the role of the cytoplasm in the execution phase. J Cell Biol 146, 703–707.

Paluch E, Piel M, Prost J, Bornens M, Sykes C (2005). Cortical actomyosin breakage triggers shape oscillations in cells and cell fragments. Biophys J 89, 724–733.

Parri M, Chiarugi P (2010). Rac and Rho GTPases in cancer cell motility control. Cell Commun Signal 8, 23.

Pato MD, Sellers JR, Preston YA, Harvey EV, Adelstein RS (1996). Baculovirus expression of chicken nonmuscle heavy meromyosin II-B. Characterization of alternatively spliced isoforms. J Biol Chem 271, 2689–2695.

Pesen D, Hoh JH (2005). Micromechanical architecture of the endothelial cell cortex. Biophys J 88, 670–679.

Pletjushkina OJ, Rajfur Z, Pomorski P, Oliver TN, Vasiliev JM, Jacobson KA (2001). Induction of cortical oscillations in spreading cells by depolymerization of microtubules. Cell Motil Cytoskeleton 48, 235–244.

Riedl J, Crevenna AH, Kessenbrock K, Yu JH, Neukirchen D, Bista M, Bradke F, Jenne D, Holak TA, Werb Z, Sixt M, Wedlich-Soldner R (2008). Lifeact: a versatile marker to visualize F-actin. Nat Methods 5, 605–607.

Robertson AM, Bird CC, Waddell AW, Currie AR (1978). Morphological aspects of glucocorticoid-induced cell death in human lymphoblastoid cells. J Pathol 126, 181–187.

Rosenfeld SS, Xing J, Chen L-Q, Sweeney HL (2003). Myosin IIB Is Unconventionally Conventional. J Biol Chem 278, 27449–27455.

Saha S, Dey SK, Biswas A, Das P, Das MR, Jana SS (2013). The effect of including the C2 insert of nonmuscle myosin II-C on neuritogenesis. J Biol Chem 288, 7815–7828.

Sahai E, Marshall CJ (2003). Differing modes of tumour cell invasion have distinct requirements for Rho/ROCK signalling and extracellular proteolysis. Nat Cell Biol 5, 711–719.

Salbreux G, Charras G, Paluch E (2012). Actin cortex mechanics and cellular morphogenesis. Trends Cell Biol 22, 536–545.

Shohet RV, Conti MA, Kawamoto S, Preston YA, Brill DA, Adelstein RS (1989). Cloning of the cDNA encoding the myosin heavy chain of a vertebrate cellular myosin. Proc Natl Acad Sci USA 86, 7726–7730.

Smutny M, Cox HL, Leerberg JM, Kovacs EM, Conti MA, Ferguson C, Hamilton NA, Parton RG, Adelstein RS, Yap AS (2010). Myosin II isoforms identify distinct functional modules that support integrity of the epithelial zonula adherens. Nat Cell Biol 12, 696–702.

Takahashi M, Kawamoto S, Adelstein RS (1992). Evidence for inserted sequences in the head region of nonmuscle myosin specific to the nervous system. Cloning of the cDNA encoding the myosin heavy chain-B isoform of vertebrate nonmuscle myosin. J Biol Chem 267, 17864–17871.

Takesono A, Heasman Sarah J, Wojciak-Stothard B, Garg R, Ridley Anne J (2010). Microtubules regulate migratory polarity through Rho/ROCK signaling in T cells. PLoS One 5, e8774.

Tinevez J Y, Schulze U, Salbreux G, Roensch J, Joanny J-F, Paluch E (2009). Role of cortical tension in bleb growth. Proc Natl Acad Sci USA 106, 18581–18586.

Trinkaus JP (1973). Surface activity and locomotion of Fundulus deep cells during blastula and gastrula stages. Dev Biol 30, 69–103.

Wang A, Ma X, Conti MA, Adelstein RS (2011). Distinct and redundant roles of the non-muscle myosin II isoforms and functional domains. Biochem Soc Trans 39, 1131–1135.

Wang F, Kovacs M, Hu A, Limouze J, Harvey EV, Sellers JR (2003). Kinetic mechanism of non-muscle myosin IIB: functional adaptations for tension generation and maintenance. J Biol Chem 278, 27439–27448.

Wolf K, Mazo I, Leung H, Engelke K, von Andrian UH, Deryugina EI, Strongin AY, Brocker E-B, Friedl P (2003). Compensation mechanism in tumor cell migration: mesenchymal-amoeboid transition after blocking of pericellular proteolysis. J Cell Biol 160, 267–277.

Yap AS, Kovacs EM (2003). Direct cadherin-activated cell signaling: a view from the plasma membrane. J Cell Biol 160, 11–16.

Yarrow JC, Totsukawa G, Charras GT, Mitchison TJ (2005). Screening for cell migration inhibitors via automated microscopy reveals a Rho-kinase inhibitor. Chem Biol 12, 385–395.